Defence Science Journal, Vol. 74, No. 2, March 2024, pp. 206-215, DOI : 10.14429/dsj.74.19626

Numerical Study on Mixing Characteristics of Circular and Non-Circular Jets

Chitimada Narendrakumar* and Kalyan Prasad Sinhamahapatra

Department of Aerospace Engineering, IIT Kharagpur - 721 302, India

**E-mail: chnarendrakumar06@gmail.com*

ABSTRACT

The study of non-circular jet flows has become important due to their various applications, such as aircraft exhaust, combustion chambers and injectors.The present paper examines the impact of elliptical, square, and triangular-shaped orifices on the mixing characteristics of a free jet with Mach number 0.8. Numerical simulations using an SST K-ω two-equation turbulence model were conducted with a Reynolds number of 3.46×10^5 for all cases. The mean velocity, decay rate, half-velocity width, spread rate, and turbulence intensity of the jet were analysed. The results showed that the triangular orifice provided the best mixing efficiency, with a shorter jet core length. The decay rate was found to be lowest for the square jet and highest for the triangular jet, which matches the previous research. The asymmetric jets experienced two axis-switching points, while the square jet experienced a 45^0 rotation of its axes but no axis-switching. The core region had lower turbulence levels, while the highest turbulence levels were in the shear layer.

Keywords: Mixing, Non-circular, Decay rate, Spread rate, Potential core, Axis-switching

NOMENCLATURE

B_e : Geometric mean of $Y_{1/2}/D_e$ and $Z_{1/2}/D_e$
D_e : Equivalent diameter
K : Turbulent Kinetic Energy
K_u : Decay rate
K_s : Spread rate
L_{pc} : Core length
RANS : Reynolds-Averaged Navier-Stokes
Red : Reynolds number
SST : Shear stress transport
U_{cl} : Orifice centerline velocity
U_e : Orifice exit velocity
X_{as}/D_e : Axis-switching location
X_v/D_e : Kinematic virtual origin
X_s/D_e : Geometric virtual origin
$Y_{1/2}/D_e$: X-Y plane half-velocity width
Z : Spanwise direction
$Z_{1/2}/D_e$: X-Z plane half-velocity width
ε : Rate of dissipation of K
ω : Specific rate of dissipation

1. INTRODUCTION

Due to the vast applications, the intricate flow patterns within turbulent free jets hold significant importance from engineering and industrial perspectives. Comprehending the mixing characteristics of turbulent free jets plays a pivotal role in advancing diverse engineering applications. Several researchers[1–4] have suggested that jets originating from non-circular geometries significantly influence their flow generation and evolution. In practical scenarios, this mixing process governs crucial aspects such as aircraft and vehicle noise reduction, pollutant dispersion in industrial zones, combustion chamber performance, and the efficacy of Heating, Ventilation, And Air Conditioning (HVAC) systems in buildings. Several researchers have suggested that jet development depends on nozzle geometry, which is the present study's primary objective. In addition to the nozzle geometry, the flow properties of turbulent jets also depend on the Reynolds number (Red) and the initial flow conditions[3-4]. As an efficient passive flow control technique, non-circular jets, like elliptical, square, triangular and rectangular jets, have gained significant importance in jet flow studies because of their mixing capabilities at a relatively lower cost. The non-circular jets have been intensively studied for several years. The main inference from these investigations is that the non-circular configurations undergo an axis-switching phenomenon.

Recently, experimental and numerical studies[1,2,5–7] confirmed that axis-switching is the flow mechanism, which is the main reason for the improved mixing of non-circular jets compared to round jets. Quinn revealed that triangular[3], elliptical[4], and rectangular[8] jets have greater jet propagation, decay rate, entrainment and larger mixing abilities in comparison to round jets. Quinn and Militzer's[9] work results showed that symmetric jets' decay and spread rates were similar, just like their potential core lengths (L_{pc}). The effect of aspect ratio on elliptical jets was investigated by Hussain and Hussain[10],who found that the location of axis-switching and elliptical jet switch overs depends on aspect ratio and initial conditions.

Over the past few years, there has been a growing trend among researchers to employ computational fluid dynamics

---

Received : 14 November 2023, Revised : 11 January 2024
Accepted : 12 January 2024, Online published : 26 March 2024

(CFD) techniques for investigating jet flow patterns and vortex structures. LES and DNS are considered the most appropriate methods for solving turbulent flows with high Red. Miller, *et al.* used DNS to study asymmetrical jets and analyzed the axis-switching phenomenon and entrainment rate details. Holdo and Simpson[12] used LES to investigate a rectangular turbulent free jet and found good agreement with experimental results in the far-field region alone. However, these computational techniques are highly expensive and take long to give the converged solution. Recently, RANS-based solvers have replaced LES and DNS in industrial and engineering applications due to their capability to simulate high Reynolds numbers with less computational time, while maintaining good accuracy.

Pope & Sarkar introduced the *K*-*ε* turbulence model with correction terms used by Thies and Tam[13] to predict the mean jet flow over different Mach numbers accurately. Meslem[14], *et al.* found that the SST *K*-*ω* turbulence model predicted the mean flow parameters, axis-switching phenomenon, and mean velocity and vorticity field for a cross-shaped orifice out of the seven turbulence models simulated, namely linear RNG, nonlinear quadratic and cubic *K*-*ε* turbulence models, *K*-*ω*, SST *K*-*ω* and RSM turbulence models. Berg et al.[15] utilised both the *K*-ε and *K*-ω models to simulate a 3D turbulent rectangular jet and found that both models successfully matched the velocity decay in the near and far-field regions when using fitted inlet velocity profiles.

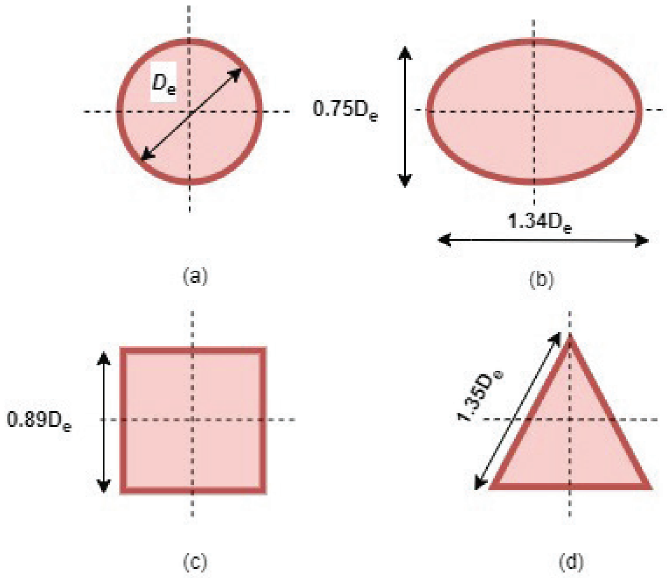

Figure 1. (a) Circular, (b) Elliptical, (c) Square, (d) Triangular orifice configurations.

In the present investigation, the jets issuing from the symmetric (circular and square jets) and asymmetric (elliptical and triangular) orifices are simulated using the RANS-based two-equation turbulence model SST *K*-*ω*. So far, experimental investigations have been carried out for each non-circular jet separately. The direct comparison between circular and non-circular jets is not extensively explored using experimental and computational techniques. Furthermore, previous investigations have only been done to investigate the mean velocity and turbulent properties and have not thoroughly investigated the decay rate, jet half-widths, and spread rate. The present study uses the two-equation turbulence modelling to predict the mixing properties in the near and far-field regions of turbulent jets. However, the circular jets are investigated in great detail; results from previous investigations with circular orifices are simulated and used for comparison purposes. The selected circular and non-circular orifice jets are simulated at a Mach number of 0.8 with the corresponding Red = 3.46×10^5. The circular orifice with a diameter of 15 *mm* and other non-circular orifices with appropriate notations are shown in Fig. 1. The chosen configurations have an outlet area (A) of 176.63 mm^2 and a mass flow rate of 0.06 kg/sec. The equivalent exit diameter (D_e) is calculated using the formula $D_e = 2\sqrt{A/\pi}$.

2. GOVERNING EQUATIONS

In this study, the dynamic flow emerging from circular, elliptical, square, and triangular jets discharges into the surrounding atmospheric field. The flow field is assumed to possess three-dimensional attributes, steady and compressible in nature. Viscosity is evaluated using the Sutherland three-coefficient formula, and density calculations are based on the ideal gas equation. Continuity, momentum, and energy equations govern the flow field, and they are given in Eqn. (1), (2) and (3).

$$\frac{\partial\left(\rho u_j\right)}{\partial x_j}=0 \quad (1)$$

$$\frac{\partial}{\partial x_j}\left(\rho u_i u_j\right)=-\frac{\partial p}{\partial x_j}+\frac{\partial}{\partial x_j}\left(\mu\frac{\partial u_j}{\partial x_j}\right)-\frac{\partial}{\partial x_j}\left(\rho\overline{u_i' u_j'}\right) \quad (2)$$

$$\frac{\partial}{\partial x_j}\left(u_j T\right)=\alpha\frac{\partial^2 T}{\partial x}-\frac{\partial}{\partial x_j}\left(\overline{u_j' T'}\right) \quad (3)$$

Where the density of the fluid is ρ, the fluid velocity is u_j, the direction coordinate is x_j, μ, and $-\rho\overline{u_i' u_j'}$ are fluid dynamic viscosity the Reynolds stress tensor. Total temperature is denoted by T, thermal diffusivity is denoted by α and turbulent heat flux is denoted $-\overline{u_j' T'}$.

The current study employs the SST *K-omega* turbulence model, which uses the *K-omega* model in close proximity to the boundaries and the *K-epsilon* model in far fields and mixing regions, as stated by Menter[16]. This model is particularly effective and precise for predicting shock waves, adverse pressure gradients and sonic flows. The present used SST *K*-*ω* model's equations are given in Eqn. (4) and (5).

Turbulent kinetic energy (*K*) transport Eqn.

$$\frac{\partial}{\partial t}\left(\rho K\right)+\frac{\partial}{\partial x_i}\left(\rho K u_i\right)=\frac{\partial}{\partial x_j}\left(\Gamma_K\frac{\partial K}{\partial x_j}\right)+\tilde{G}_K -Y_K+S_K \quad (4)$$

Turbulent kinetic energy dissipation (*ω*) transport Eqn.

$$\frac{\partial}{\partial t}\left(\rho\omega\right)+\frac{\partial}{\partial x_i}\left(\rho\omega u_i\right)=\frac{\partial}{\partial x_j}\left(\Gamma_\omega\frac{\partial\omega}{\partial x_j}\right)+\tilde{G}_\omega -Y_\omega+D_\omega+S_\omega \quad (5)$$

Effective diffusivity of *k* and ω are represented by Γ_k and

Γ_ω, respectively.

$$\Gamma_K = \mu + \frac{\mu_t}{\sigma_K},\ \Gamma_\omega = \mu + \frac{\mu_t}{\sigma_\omega} \tag{6}$$

Here, turbulent Prandtl numbers for K and ω are given by σ_K and σ_ω respectively. The turbulent viscosity, μ_t, is calculated using the below equation

$$\mu_t = \frac{\rho K}{\omega}\frac{1}{\max\left[\frac{1}{\alpha^*},\frac{SF_2}{a_1\omega}\right]} \tag{7}$$

The strain rate magnitude is given by S

$$\sigma_K = \frac{1}{F_1/\sigma_{K,1} + \left(1-F_1\right)/\sigma_{K,2}} \tag{8}$$

$$\sigma_\omega = \frac{1}{F_1/\sigma_{\omega,1} + \left(1-F_1\right)/\sigma_{\omega,2}} \tag{9}$$

$$\alpha^* = \alpha^*_\infty \frac{\alpha^*_0 + Re_t/R_K}{1+Re_t/R_K},\ R_t = \frac{\rho K}{\mu\omega},\ \alpha^*_0 = \frac{\beta_i}{3} \tag{10}$$

F_1 and F_2 are blending functions, and these are given as follows:

$$F_1 = \tanh\left(\Phi_1^4\right) \tag{11}$$

$$\Phi_1 = \min\left[\max\left(\frac{\sqrt{K}}{0.09\omega y},\frac{500\mu}{\rho y^2\omega}\right),\frac{4\rho K}{\sigma_{\omega,2}D^+_\omega y^2}\right] \tag{12}$$

$$D^+_\omega = \max\left[2\rho\frac{1}{\sigma_{\omega,2}}\frac{1}{\omega}\frac{\partial K}{\partial x_j}\frac{\partial\omega}{\partial x_j},10^{-10}\right] \tag{13}$$

$$F_2 = \tanh\left(\Phi_2^2\right) \tag{14}$$

$$\Phi_2 = \max\left[2\frac{\sqrt{K}}{0.09\omega y},\ \frac{500\mu}{\rho y^2\omega}\right] \tag{15}$$

The blending function is formulated to be unity in the wall's proximity, triggering the standard K-ω model while transitioning to zero farther from the surface, activating the transformed K-ε model.

Production of turbulence kinetic energy term G_K is given as follows:

$$G_K = \min\left(G_K, 10\rho\beta^* K\omega\right) \tag{16}$$

$$G_k = -\rho u'_i u'_j \frac{\partial u_j}{\partial x_i} \tag{17}$$

Production of dissipation in K, G_ω is given by:

$$G_\omega = \frac{\alpha}{\nu_t}\tilde{G}_K \tag{18}$$

α_∞ is given by:

$$\alpha_\infty = F_1\alpha_{\infty,1} + \left(1-F_1\right)\alpha_{\infty,2} \tag{19}$$

Here,

$$\alpha_{\infty,1} = \frac{\beta_{i,1}}{\beta^*_\infty} - \frac{K^2}{\sigma_{\omega,1}\sqrt{\beta^*_\infty}} \tag{20}$$

$$\alpha_{\infty,2} = \frac{\beta_{i,2}}{\beta^*_\infty} - \frac{K^2}{\sigma_{\omega,2}\sqrt{\beta^*_\infty}} \tag{21}$$

where K is 0.41.

The dissipation of turbulence kinetic energy is denoted by Y_K here.

$$Y_k = \rho\beta^* k\omega \tag{22}$$

The term Y_ω represents the dissipation of ω.

$$Y_\omega = \rho\beta w^2 \tag{23}$$

$$\beta_i = F_1\beta_{i,1} + \left(1-F_1\right)\beta_{i,2} \tag{24}$$

D_ω represents the cross-diffusion term

$$D_\omega = 2\left(1-F_1\right)\rho\sigma_{\omega,2}\frac{1}{\omega}\frac{\partial K}{\partial x_j}\frac{\partial\omega}{\partial x_j} \tag{25}$$

Model Constants

$$\sigma_{K,1} = 1.17,\ \sigma_{\omega,1} = 2.0,\ \sigma_{K,2} = 1.0,$$
$$\sigma_{\omega,2} = 1.168,\ a_1 = 0.31,\ \beta_{i,1} = 0.075,$$
$$\beta_{i,2} = 0.0828,\ \alpha^*_\infty = 1,\ \alpha_\infty = 0.52,$$
$$\alpha_0 = \frac{1}{9},\ \beta^*_\infty = 0.09,\ \beta_i = 0.072,$$
$$R_\beta = 8,\ R_K = 6,\ R_\omega = 2.95$$

3. NUMERICAL DETAILS

This study solved the flow field governing equations (continuity, momentum and energy) using the finite volume-based computational tool ANSYS Fluent 19.2 R2. The present investigation used the pressure-based coupled algorithm[17] to solve the system of equations comprising the momentum and continuity equations. This coupled algorithm improves the convergence significantly as compared to another pressure-based segregated algorithm. Rhie-Chow interpolation[18] method was implemented to avert oscillations of pressure. A bounded QUICK scheme[19] was used to discretize the convection terms. The second-order central differencing scheme resolves the viscous terms, and the pressure-velocity coupling follows the SIMPLEC procedure with a skewness correction of 1. Double precision solver solves the round-off errors generated by the supercomputer during the iterative process. Under-relaxation factors for momentum and pressure were established at 1 and 1, respectively. The simulations were iterated until convergence of outcomes was attained. Convergence of residuals was deemed reached when the absolute values of pressure, temperature, and velocity components were below 10^{-6} within the iterative solution process.

The computational flow domain had a size of 30De × 5.3De × 5.3De in X, Y and Z directions. The boundary conditions applied to the flow domain are shown in Fig. 2. At the domain inlet, a pressure inlet boundary condition was provided with a stagnation pressure of 154 KPa and a stagnation temperature of 300 K. In the far field, pressure inlet boundary conditions were applied, prescribing a total pressure of 101325 Pa and an ambient temperature of 300 K. The outlet condition was defined as a pressure outlet, with atmospheric pressure and temperature values assigned. The current study set the ambient/atmospheric pressure and temperature to 101,325 Pa and 300 K, respectively.

4. RESULTS AND DISCUSSIONS

4.1 Grid Sensitivity and Validation

Due to strong velocity gradients in the flow direction, an unstructured mesh discretises the flow region. An unstructured

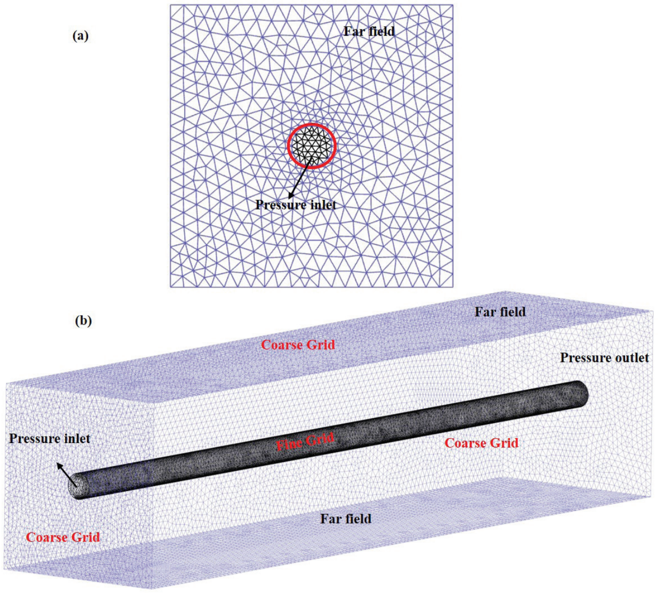

Figure 2. Coarse mesh (a) near circular orifice jet exit and (b) of computational domain.

mesh with tetrahedral elements generated with various mesh techniques available in the ANSYS workbench mesh generation tool was used in the computational domain. Fine grids are employed at the jet boundary to model the jet shear layer and potential core region. Figure 2 presents the unstructured coarse mesh at a cross-section near the circular orifice jet exit and the mesh structure of the computational domain. The grid sensitivity of the predicted solution is checked using four grids with 0.8, 1.6, 2.7, 3.3, and 3.7 million cells. The circular jet's centerline velocity (U_{cl}) was plotted against the axial distance in the grid test to identify the appropriate mesh. Almost identical results were obtained with meshes that contained 2.7 million or more elements; therefore, the mesh size for the present study was fixed at 2.7 million.

The predicted circular jet result was validated with the available experimental[20], and numerical[21] results from the literature. Figure 3 shows the mean centerline velocity decay in the streamwise direction against the X/D_e ratio. From Fig. 3, it is evident that the present used SST K-ω turbulence model could accurately envisage the mean velocity decay of a circular jet. The turbulence model employed in this study demonstrated excellent agreement with experimental[20] values up to 10 jet diameters. However, after this distance, the decay predicted by the present turbulence model slightly underestimates experimental observations. Nevertheless, the simulated circular jet result at Mach 0.8 is qualitatively consistent with the LES[21]and DNS[21] results obtained at Mach 0.9. Therefore, the SST *K-omega* turbulence model utilized in this study proves to be effective in simulating both axis-symmetric and asymmetrical jets.

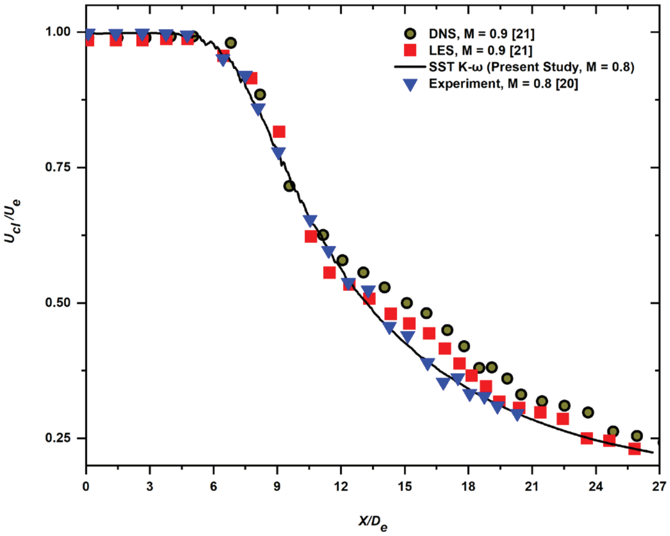

Figure 3. Streamwise centerline velocity decay of circular jet.

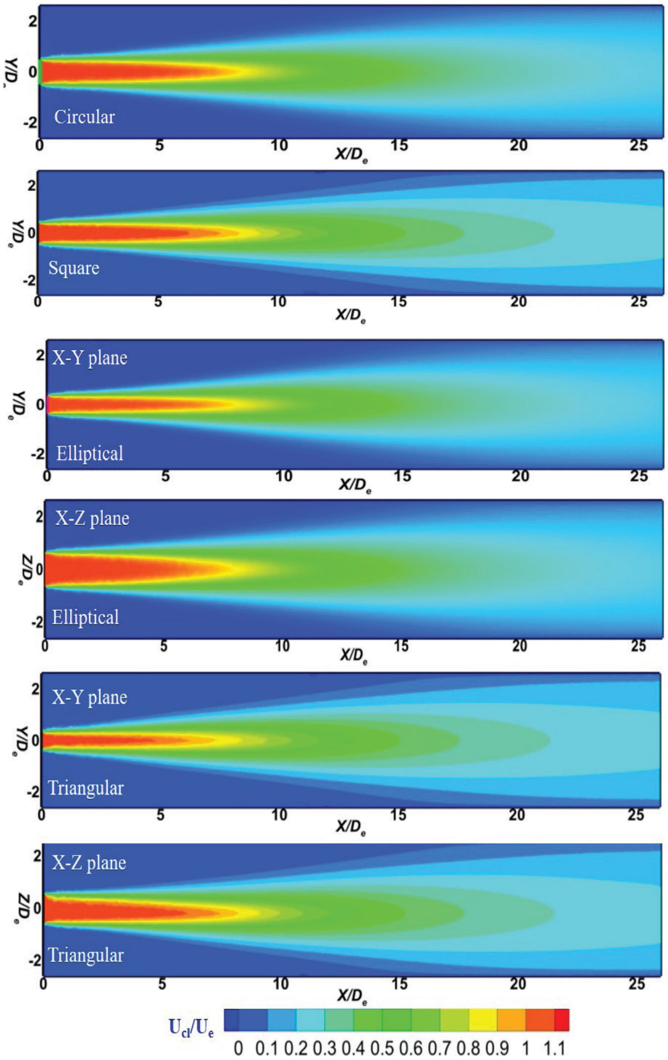

Figure 4. Normalised mean velocity contour plots.

4.2 Mean Centerline Velocity Decay

Figure 4 shows the contour plots of the normalized centerline mean velocity (U_{cl}/U_e) for circular and non-circular jets. The centerline velocity and streamwise distance are non-dimensionalized by exit velocity at the orifice (U_e) and equivalent diameter (D_e). From Fig. 4, it is understood that shortly after exiting from the orifice, the flow accelerates and attains its peak velocity due to the vena contracta effect. Initially, the jet contour levels are relatively small and close, but the distance between the contour levels increases far downstream. This is owing to the enhanced entrainment of surrounding atmospheric fluid into the core jet. Owing to this enhanced entrainment, the jet grows linearly, and the contour levels in between distance increases. In addition, the circular and square jets were similar in their jet spread and decay. Nevertheless, the elliptical and triangular jets encountered distinct variations in their spread and decay rates along the streamwise distance. It can also be noted from Fig. 4 that the flow features of elliptical and triangular jets differ due to the asymmetry of their cross-sectional shape[1,3,4,6]. Furthermore, the elliptical jet exhibits a greater thickness in the X-Z plane than the other jets. The variation in thickness between the X-Z and X-Y planes of the elliptical jet is attributed to the differential spreading occurring along its major and minor axes.

A subsonic flow consists of three distinct regions in its flow field as it propagates downstream. A potential core is a region with constant velocity up to a certain distance downstream from the nozzle/orifice exit. The mean velocity along the centerline tends to decrease in the subsequent region as the surrounding fluid interacts with the jet fluid, and this region is termed the transition region or characteristic decay region. At last, the centerline velocity decay is minimal, and the jet fluid behaves like an atmospheric fluid in the far field. This region is called the fully developed region. The velocity profile at different locations was found to be identical in this region. Hence, this region can also be called a self-similar region.

In general, jet mixing characteristics are quantified by analysing the centerline velocity decay plot. Fig. 5 compares the streamwise centerline velocity decay of investigated jets at Mach number 0.8. The potential core length (L_{pc}) of square and circular extended up to $X/D_e = 5.8$ from the orifice exit. Similarly, the L_{pc} of elliptical and triangular jets was preserved up to $X/D_e = 5.2$ and 4.3, respectively. In the transition region, the distinguishing regions of decay were found for the jets investigated. For example, symmetric jets only undergo an axisymmetric decay, while elliptical and triangular jets have two distinct decay regimes, such as axisymmetric and characteristic decay[22]. In these characteristic and axisymmetric decay regions, the mean centerline velocity decay in the flow direction is inversely proportional to the downstream distance from the orifice exit. From the circular and non-circular jets currently being studied, elliptical and triangular jets have improved mixing proper ties than symmetrical jets. The square and circular jets displayed the same behaviour in all regions. From Fig. 5, the characteristic decay region is observed between $X/D_e = 5.8$ to 12 for axisymmetric jets, and between $X/D_e = 5$ to 10 for elliptical and triangular jets. After $X/D_e = 10$, the jet profile for all jets was found to be similar from $X/D_e = 15$ onwards; hence, this region is called a fully developed region. The percentage reduction in L_{pc} for non-circular jets with respect to circular jet was calculated using the following Eqn. (26).

Per cent reduction in potential core length

$$= \frac{\left[\left(L_{pc}\right)_{cj} - \left(L_{pc}\right)_{ncj}\right]}{\left(L_{pc}\right)_{cj}} \times 100 \qquad (26)$$

The L_{pc} of circular and non-circular jets are denoted by $(L_{pc})_{cj}$ and $(L_{pc})_{ncj}$, respectively. Among the orifice geometries studied, the triangular jet reduced the initial core length, and the velocity drop for the triangular orifice was higher than the other jets. The maximum reduction in L_{pc} was 26 % for the triangular jet, whereas the elliptical jet core length was reduced by 10 %. Out of the tested orifice geometries, the triangular jet promoted mixing efficiency better than the other jets. The axis-switching phenomenon contributes to improved mixing in non-circular jets[2–4,9,13]. The present obtained L_{pc} and literature works are presented in Table 1. It is noted from Table 1 that the non-circular jets L_{pc} obtained by the present numerical simulation matches the previous experimental[3-4,10,20,23-24] and numerical works[29].

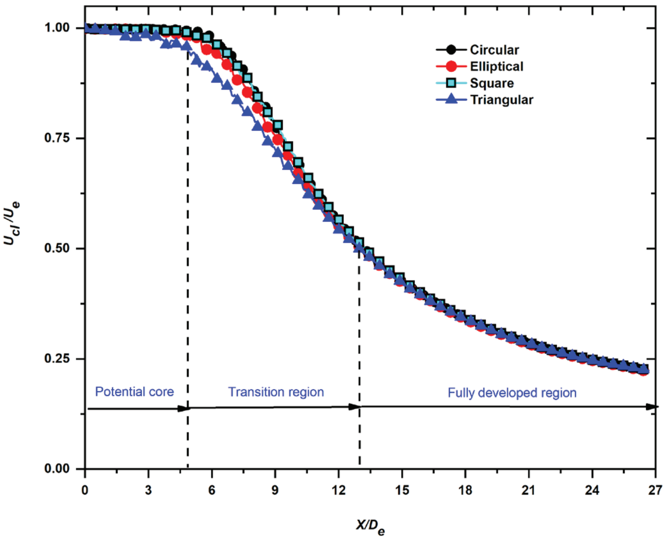

Figure 5. Mean centerline velocity decay of simulated jets.

4.3 Jet Decay Rate

The jet emerging from the orifice exit enters the atmosphere, mixes with the atmospheric fluid, and propagates, causing the velocity to decrease with the streamwise distance. In addition to L_{pc}, the velocity decay rate is also generally employed to understand the mixing of the jet with the surrounding fluid. The following Eqn. (27) is used to calculate the decay rate in the present study.

$$\frac{U_e}{U_{cl}} = K_u\left(\frac{X - x_v}{D_e}\right) \qquad (27)$$

Here, the decay rate and kinematic virtual origin are denoted by K_u and X_v/D_e, respectively. Jet exit conditions determine K_u and X_v/D_e values. The Eqn. (27) is technically valid only in the far-field region, but several researchers[3, 23, 24] also used it in the transition region to calculate the decay rates.

Jet decay rate is generally calculated by plotting the reciprocal profile U_{cl}/U_e. The decay rate values for all models are calculated within the X_v/D_e range of 6 to 26. The K_u values of the presently studied jets, along with the previous experimental and numerical results, are presented in Table 1. The decay rates of the circular, elliptical, square and triangular jets are 0.180,0.189, 0.179, and 0.202, respectively. The results indicate that the K_u is lowest for the square jet, followed by the circular jet.

Table 1. Potential core length and decay rates of present simulated jets along with literature

Author	**Shape**	L_{pc}	K_u	X_v/D_e	**Red (×10^5)**
Present	Circular	5.80	0.180	-0.316	3.46
Present	Elliptical	5.20	0.189	-0.372	3.46
Present	Square	5.80	0.179	-0.313	3.46
Present	Triangular	4.30	0.202	-0.382	3.46
Quinn[3]	Circular	3.50	0.205	2.167	1.84
Quinn[3]	Triangular	2.95	0.207	-0.181	1.84
Quinn[4]	Elliptical	2.83	0.184	-0.426	1.88
Quinn & Miltzer[9]	Square	-	0.185	-0.150	1.84
Hussain[10]	Elliptical	3.00	0.164	0.030	1.00
Thangaraj & Kaushik[20]	Circular	3.40	-	-	4.08
Thangaraj & Kaushik[20]	Elliptical	2.80	-	-	4.08
Thangaraj & Kaushik[20]	Square	3.40	-	-	4.08
Mi & Nathan[23]	Circular	5.60	-	-	0.15
Mi & Nathan[23]	Elliptical	3.10	-	-	0.15
Mi & Nathan[23]	Square	3.20	-	-	0.15
Mi & Nathan[23]	Triangular	3.00	-	-	0.15
Hashiehbaf & Romano[24]	Elliptical	3.20	-	-	0.35
Hashiehbaf & Romano[24]	Square	3.81	-	-	0.35
Hashiehbaf & Romano[24]	Triangle	3.60	-	-	0.35
Kumar & Sinhamahapatra[29]	Circular	6.00	0.180	-0.310	3.46
Kumar & Sinhamahapatra[29]	Elliptical	5.40	0.184	0.340	3.46

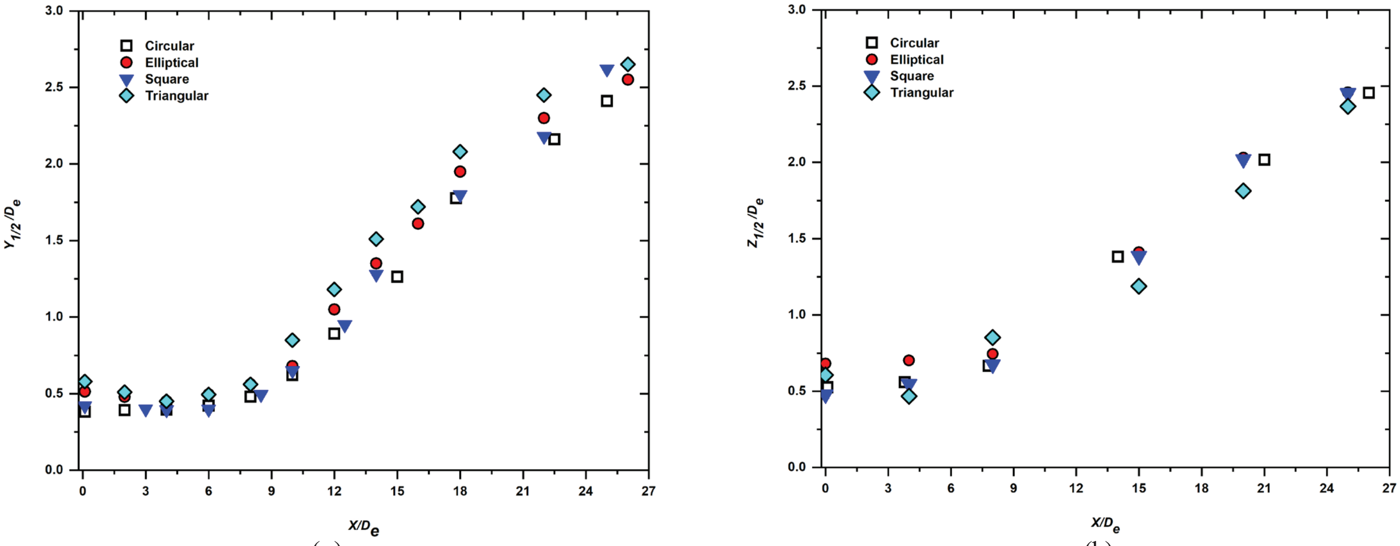

(a) (b)

Figure 6. Development of half-velocity widths in (a) X-Y (b) X-Z planes.

The triangular jet had a higher K_u value than the other jets, indicating that the mixing efficiency was likely to be the highest. In addition, elliptical and triangular jets show higher decay rates than axisymmetric circular and square jets. Table 1 shows that the values obtained in the current study are in good agreement with the literature. Table 1 also shows this study's kinematic virtual origin values, along with the literature. The values of X_v/D_e follow a similar trend of the decay rate. The X_v/D_e value is higher for a triangle jet and lower for a square jet. The values of X_v/D_e in current and previous studies show a significant difference, even when the orifice geometry is similar. This suggests that the X_v/D_e is greatly influenced by the jet's initial conditions (shape and geometry).

4.4 Jet Half-Velocity Width and Spread Rate

Along with L_{pc} and decay rate, the half velocity widths are commonly used to study jet spreading in the downstream locations. As defined by Quinn[4] the half-velocity width refers to the distance across a jet flow field, measured perpendicular to the jet's axis, where the velocity of the fluid is half of its maximum value. It is a crucial parameter used to characterize the spatial extent of a jet and provides insights into its mixing behaviour and the distribution of fluid velocities across its cross-section. Figure 6 illustrates the half-velocity width profiles in the X-Y and X-Z planes from the origin. $Y_{1/2} / D_e$ represents the half-velocity width in the X-Y plane, and $Z_{1/2} / D_e$ represents the half-velocity width in the X-Z plane. There is a consistent growth in half-velocity width with distance from the orifice exit for circular and square jets in the X-Y and X-Z planes. However, for elliptic and triangular jets, the half-velocity widths in the X-Z plane follow a similar trend as circular and square jets. Conversely, within the X-Y plane, the half-velocity widths follow an initial decrease followed by a continuous increase, attributed to the differential spreading across the major and minor axes.

This behavior of elliptical and triangular jets in both the X-Y and X-Z planes is directly associated with the occurrence of axis-switching phenomena. In an elliptical jet, as the jet progresses downstream, the primary vortex structures may initially align with the ellipse's major axis but then switch to aligning with the minor axis. This phenomenon is called axis-switching. The elliptical jet switches its minor and major axes several times along the flow direction until damped.

Similarly, in a triangular jet, the primary vortices are initially aligned with one of the triangular jet's edges. However, the alignment can shift to a different edge as the jet progresses. This transition in the alignment of the vortices is also known as axis-switching in the triangular jet. The location of the axis-switching (X_{as}/D_e) depends on the jet's initial conditions, jet shape and forcing[1,2,9,26]. According to Gut mark and Ho[25], vortex rings at the edges of non-circular jets behave differently in minor and major directions. Due to Kelvin-Helmholtz's instability, these vortex rings initially roll up at the orifice location and contract in the X-Z plane. On the other hand, in the X-Y plane, the vortex rings expand first in the direction of flow and then shrink as distance increases. The Biot-Savart law dictates how such circumferential vortex rings deform, at least in the jet near field. These distinct flow features of asymmetric jets in the X-Y and X-Z planes are attributed to the axis-switching phenomena.

The elliptical jet experienced two axis-switching locations; the first is within the streamwise distance of 3 to 5 (Fig. 6(a)), and the other is after X/D_e>18. The first axis-switching formation in an elliptical jet with mean velocity contours can be seen Fig. 7(a). These mean velocity contours at different axial locations are in line with the evolution of an elliptic jet in the flow direction studied by Miller[11], *et al.* From Figure, at the jet exit or near the nozzle (X/D_e=2), the primary

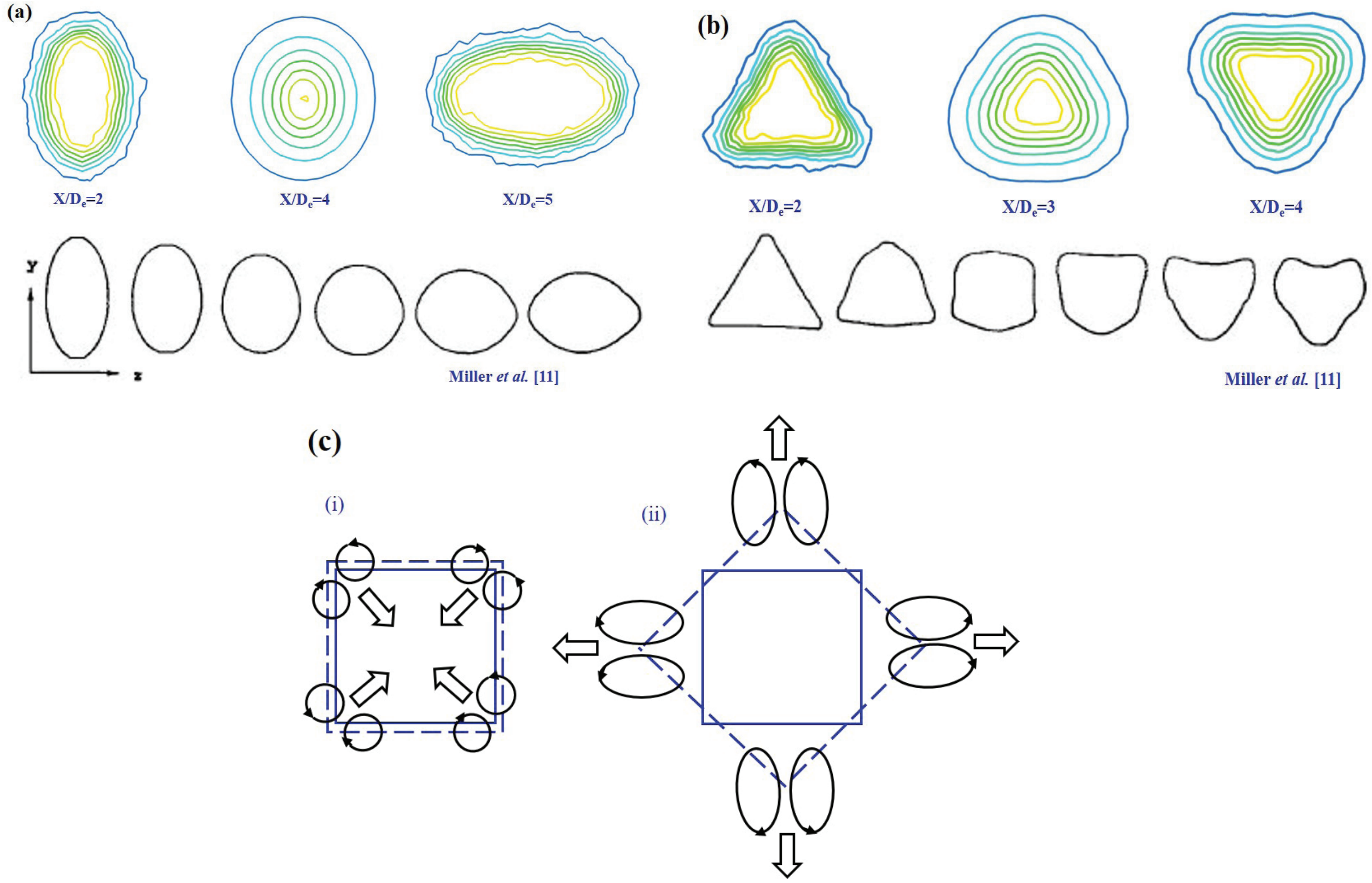

Figure 7. Axis-switching phenomena in non-circular jets; (a) Mean velocity contours of elliptical jet; (b) Mean velocity contours of triangular jet; and (c) Evolution of square jet (i) near the jet exit, (ii) downstream location.

vortex structures are aligned with either the major or minor axis of the elliptical cross-section. As the jet moves downstream, there is a transition zone where the orientation of the vortices starts to change. This is the region where the alignment of the vortices switches from one axis to the other. This transition is observed between X/D_e=4-5 for the elliptic jet, which is seen in Fig. 7(a). In this region, the vortex structures gradually reorient themselves to align with the other axis of the ellipse. This reorientation results in a change in the overall flow patterns and mixing features of the jet.

The triangular jet also showed two axis-switching locations; the first axis-switching occurred between the X/D_e range of 2 to 4, and the second switch between 14 to 16. The formation of the first axis-switching was depicted in Fig. 7(b). In a triangular jet, the primary vortex structures align with one of the edges of the triangular cross-section, whereas these structures align with either the major or minor axis of the elliptical cross-section. As the triangular jet advances downstream, the vortex structures change and gradually shift from one edge to another. This process goes on until the vortex structures stabilize with their alignment. Coming to square jet, it did not show any axis-switching but has undergone a 45^0 rotation of its axes in the downstream locations. Due to its symmetric shape and equal-length sides, a square jet typically does not exhibit axis-switching phenomena. This is primarily because the vortex structures in a square jet remain aligned with the sides of the square as the jet progresses downstream, and this can be seen in Fig. 7(c). Unlike elliptical or triangular jets, where the alignment of the vortex structures can switch between major and minor axes or different edges, a square jet's symmetrical geometry maintains a consistent alignment of vortices along its sides. Though there is no axis-switching in square jet, this 45° rotation played a significant role in jet mixing, velocity decay, and spread rates. The X_{as}/D_e obtained in the present numerical study match previous studies[1–4,7,9–11,23,28-29]. In the overall sense, both elliptical and triangular jets experience axis-switching due to the differential spreading along their axes and the changing flow conditions as the jets move downstream.

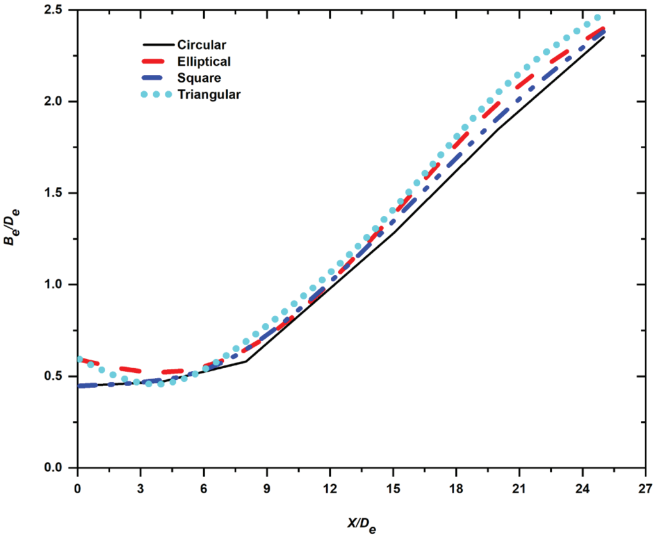

Figure 8. Geometric mean of the half-velocity widths.

The spread rate for the present studied orifices is calculated by the geometric mean of the half velocity widths, $B_e=(Y_{1/2}Z_{1/2})^{0.5}$. The B_e provides a clear assessment for estimating the spread rates of the circular and non-circular jets. For the present study,the spread rate is calculated by fitting the following Eqn. (28) to the geometric mean of the half-velocity width profile, i.e., presented in Fig. 8.

$$\frac{B_e}{D_e}=K_s\left(\frac{X-x_s}{D_e}\right) \tag{28}$$

Here, the spread rate is denoted by K_s, and X_s denote the geometric virtual origin.The spread rates are calculated in the $8<X/D_e<26$ streamwise range. From Fig. 8, the spread rate was higher for the triangular jet and smaller for circular and square jets, an observation that is consistent with the literature. In addition, the K_s of the square jet is similar to the circular jet. Table 2 summarizes this study's results and the spread rates of non-circular jets reported in previous experimental[3-4,9-10,26] and numerical[29] studies. While the spread rate variations among the simulated jets are minimal due to their calculation being confined to the transition region, the geometric virtual origin values exhibit more significant differences, indicating the sensitivity of X_s to jet configuration and initial conditions.

Table 2. Spread rate and geometric virtual origin

Author	Shape	K_s	X_s/D_e	Range (X/D_e)	Red($\times10^5$)
Present	Circular	0.1067	−0.2735	8 - 26	3.46
Present	Elliptical	0.1076	−0.2124	8 - 26	3.46
Present	Square	0.1078	−0.2717	8 - 26	3.46
Present	Triangular	0.1081	−0.1806	8 - 26	3.46
Quinn[3]	Circular	0.0911	−0.0956	10 - 20	1.84
Quinn[4]	Elliptical	0.0972	0.1273	10 - 20	1.84
Hussain[10]	Elliptical	0.1037	−0.0588	16 - 57	1.88
Quinn & Miltzer[9]	Circular	0.091	-1.02	9.8 - 22.4	1.84
Quinn & Miltzer[9]	Square	0.087	0.650	9.8 - 22.4	1.84
Ho & Gutmark[27]	Elliptical	0.1306	-0.216	7 - 22	0.78
Kumar & Sinhamahapatra[29]	Circular	0.963	-	6 - 26	3.46
Kumar & Sinhamahapatra[29]	Elliptical	0.100	-	6 - 26	3.46

4.5 Turbulent Intensity on Jet Centerline

Achieving high turbulent intensity in non-circular jets contributes to greater flow mixing. Streamwise turbulent intensity contours of present simulated jets are shown in Fig. 9. For all configurations, higher turbulence levels are seen within the shear layer near half-velocity width and lower levels are seen in the core region. Observed high turbulence levels in shear layers are due to the development of vortical structures due to the K-H instability. It is well known that the potential core end is where maximum mixing is expected to occur on the jet centerline. From Fig. 9, it is evident that the triangular jet experiences earlier mixing than the other jets, which is

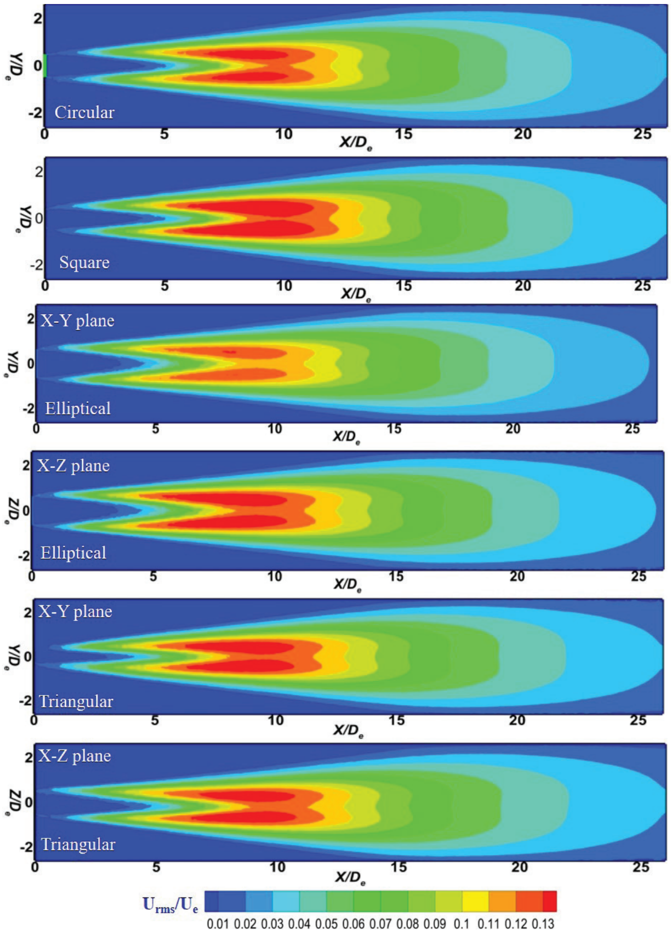

Figure 9. Contours of turbulent intensity in the streamwise direction.

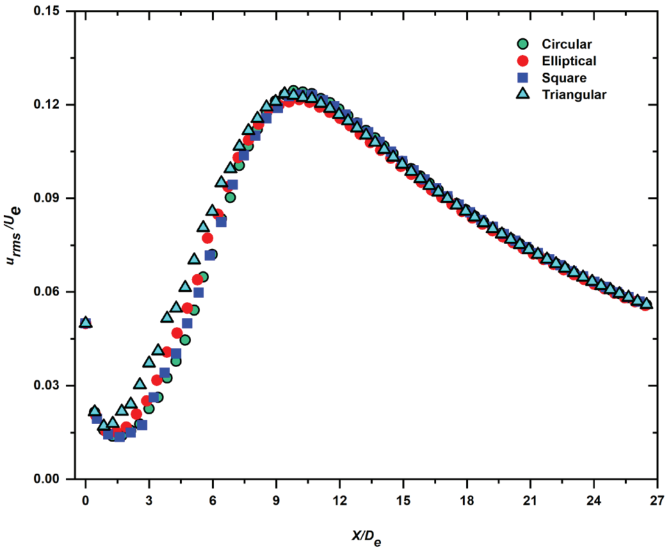

Figure 10. Streamwise turbulence intensity on jet centerline.

confirmed by the shorter L_{pc} of the triangular jet. Also, the elliptical jet experienced earlier mixing than the other jets after the triangular jet. As the jet propagates further downstream, peaks in turbulent intensity begin to propagate in the jet streamwise, lateral and spanwise directions. Additionally, square and triangular jets cover a large area with the greatest intensity of turbulent activity.

The streamwise turbulent intensities on the jet centerline are presented in Fig. 10. From Fig. 10, till $X/D_e = 9$, the triangular jet experienced the highest turbulence intensity, followed by the elliptical jet. Within this distance, the turbulent intensity of circular and square jets is approximately close to each other. For all configurations, streamwise turbulence intensities at the jet centerline increased rapidly and reached peak values of u_{rms}/U_e within the X/D_e range of 9 to 11. This illustrates that higher turbulence levels occurred after Lpc and appear to have a stronger association with X_{as} as opposed to the vena contracta impact. After the peak values, all configurations have shown similar turbulence levels.

5. CONCLUSIONS

The circular and non-circular jets mixing behaviour was studied numerically using the RANS-based two-equation turbulence model SST K-ω. Non-circular jets (ellipse, square, and triangular) were compared to circular jets to evaluate their mixing characteristics. The simulations were conducted at a Mach number of 0.8 and a Reynolds number of 3.46×10^5.

The vena-contracta phenomenon and axis-switching (in the non-circular shape) phenomenon were observed. The triangular jet's potential core length was shortened by 26 % compared to the circular jet, indicating that mixing was superior for the triangular jet. The results showed that the triangular jet mixes better with atmospheric fluid out of the investigated jets, followed by the elliptical jet, verified by shorter L_{pc}, K_s, and higher K_u. The axis-switching phenomenon was seen in the elliptical and triangular jets, while the square jet had undergone 45 degree rotation in the downstream locations. Furthermore, at the jet exit, each configuration contour and profile plots showed low levels of turbulent intensity in the core region. After that, the turbulent intensity diffused toward the jet centerline, attaining peak values within the X/D_e range of 9 to 11.

REFERENCES

1. Grinstein, F.F.; Gutmark, E. & Parr, T. Near field dynamics of subsonic free square jets. A computational and experimental study. *Phys. Fluids*, 1995, **7**(6), 1483-1497.
   doi: 10.1063/1.868534
2. Gutmark, E.J. & Grinstein, F.F. Flow control with noncircular jets. *Annu. Rev. Fluid Mech,* 1999, **31**(1), 239-272.
   doi: 10.1146/annurev.fluid.31.1.239
3. Quinn, W.R. Measurements in the near flow field of an isosceles triangular turbulent free jet. *Exp. Fluids*, 2005, **39**, 111-126.
   doi:10.1007/s00348-005-0988-2
4. Quinn, W.R. Experimental study of the near field and transition region of a free jet issuing from a sharp-edged elliptic orifice plate. *Euro. J. Mech B/Fluids*, 2007, **26**(4), 583-614.
   doi: 10.1016/j.euromechflu.2006.10.005
5. Grinstein, F.F. Vortex dynamics and entrainment in rectangular free jets. *J. Fluid Mech.*, 2001, **437**, 69-101.
   doi: 10.1017/S0022112001004141
6. Zaman, K.B.M.Q. Axis switching and spreading of an

asymmetric jet: the role of coherent structure dynamics. *J. Fluid Mech.*, 1996, **316**, 1-27.
doi: 10.1017/S0022112096000420

7. Yoon, J.H., & Lee, S.J. Investigation of the near-field structure of an elliptic jet using stereoscopic particle image velocimetry. *Meas. Sci. Technol*, 2003, **14**(12), 2034.
doi:10.1088/0957-0233/14/12/002
8. Quinn, W.R. Development of a large-aspect-ratio rectangular turbulent free jet. *AIAA J.*, 1994, 32(3), 547–554.
doi: 10.2514/3.12020
9. Quinn, W.R., & Militzer, J. Experimental and numerical study of a turbulent free square jet. *Phys. Fluids*, 1988, **31**(5), 1017-1025.
doi: 10.1063/1.867007
10. Hussain, F. & Husain, H.S. Elliptic jets. Part 1. Characteristics of unexcited and excited jets. *J. Fluid Mech.*, 1989, **208**, 257-320.
doi: 10.1017/S0022112089002843
11. Miller, R.S.; Madnia, C.K. & Givi, P. Numerical simulation of non-circular jets. *Comp. & Fluids*, 1995, **24**(1), 1-25.
doi: 10.1016/0045-7930(94)00019-U
12. Holdø, A.E. & Simpson, B.A.F. Simulations of high-aspect-ratio jets. *Int. J. Numer. Methods Fluids*, 2002, **39**(4), 343-359. doi: 10.1002/fld.340
13. Thies, A.T. & Tam, C.K. Computation of turbulent axisymmetric and non-axisymmetric jet flows using the K-epsilon model. *AIAA J.*, 1996, **34**(2), 309-316.
doi: 10.2514/3.13065
14. Meslem, A.; Bode, F.; Croitoru, C. & Nastase, I. Comparison of turbulence models in simulating jet flow from a cross-shaped orifice. *Euro. J. Mech B/Fluids*, 2014, **44**, 100-120.
doi: 10.1016/j.euromechflu.2013.11.006
15. Berg, J. R.; Ormiston, S. J. & Soliman, H.M. Prediction of the flow structure in a turbulent rectangular free jet. *Int. Commun. Heat Mass Transf.***,** 2006, **33**(5), 552-563.
doi: 10.1016/j.icheatmasstransfer.2006.02.007
16. Menter, F.R. Two-equation eddy-viscosity turbulence models for engineering applications. *AIAA J.*, 1994, **32**(8), 1598-1605.
doi: 10.2514/3.12149
17. Patankar, S.V. Numerical heat transfer and fluid flow. CRC press, 2018.
doi: 10.1201/9781482234213
18. Rhie, C.M. & Chow, W.L. Numerical study of the turbulent flow past an airfoil with trailing edge separation. *AIAA J.*, 1983, **21**(11), 1525-1532.
doi: 10.2514/3.8284
19. Leonard, B.P. A stable and accurate convective modelling procedure based on quadratic up stream interpolation. *Comput. Methods Appl. Mech. Eng.*, 1979, **19**(1), 59-98.
doi: 10.1016/0045-7825(79)90034-3
20. Thangaraj, T. & Kaushik, M. Effects of circular and non-circular nozzle exit geometries on subsonic and supersonic jet propagations. *Proc. Inst. Mech. Eng. G.*, 2023, **237**(1), 209-229. doi: 10.1177/09544100221097537
21. Freund, J. Acoustic sources in a turbulent jet-A direct numerical simulation study. *In* 5th AIAA/CEAS Aeroacoustics Conference and Exhibit 1998, 1858.
22. Trentacoste, N. & Sforza, P. Further experimental results for three-dimensional free jets. *AIAA J.*, 1967, **5**(5), 885-891.
doi: 10.2514/3.4096
23. Mi, J. & Nathan, G.J. Statistical properties of turbulent free jets issuing from nine differently-shaped nozzles. *Flow Turbul. Combust.*, 2010, **84**, 583-606.
doi: 10.1007/s10494-009-9240-0
24. Hashiehbaf, A. & Romano, G.P. Particle image velocimetry investigation on mixing enhancement of non-circular sharp edge nozzles. *Int. J. Heat Fluid Flow*, 2013, **44**, 208-221.
doi: 10.1016/j.ijheatfluidflow.2013.05.017
25. Gutmark, E. & Ho, C.M. Visualization of a forced elliptic jet. *AIAA J.*, 1986, **24**(4), 684-685.
doi: 10.2514/3.9328
26. Koshigoe, S. Gutmark, E., Schadow, K.C. & Tubis, A. Initial development of noncircular jets leading to axis switching. *AIAA J.*, 1989, **27**(4), 411-419.
doi: 10.2514/3.10128
27. Ho, C.M., & Gutmark, E. Vortex induction and mass entrainment in a small-aspect-ratio elliptic jet. *J. Fluid Mech.*, 1987, **179**, 383-405.
doi: 10.1017/S0022112087001587
28. Gohil, T. B., Saha, A.K. & Muralidhar, K. Direct numerical simulation of free and forced square jets. *Int. J. Heat Fluid Flow*, 2015, ***52***, 169-184.
doi: 10.1016/j.ijheatfluidflow.2015.01.003
29. Kumar, N. & Sinhamahapatra, K.P. The effects of spacing to diameter ratio on mixing characteristics of circular and elliptical twin jets. *Proc. Inst. Mech. Eng. G.,* 2023, **237**(11), 2632-2646.
doi:10.1177/09544100231155692

CONTRIBUTORS

Mr Chitimada Narendrakumar is a Doctoral Student in the Aerospace Engineering Department at IIT Kharagpur. He completed his Master's and Bachelor's at MIT campus, Anna university and JNTU Kakinada. His research interests include High-speed aerodynamics, jet flow control, CFD and turbulent flows.
His contributions to the present study are carrying out the simulations, methodology, post-processing the results, and writing the original manuscript.

Dr Kalyan Prasad Sinhamahapatra is a HAL Chair Professor in the Aerospace Engineering Department, IIT Kharagpur. His areas of interest comprise Computational fluid dynamics, large eddy simulation, aeroacoustics and fluid-structure interaction. This research was carried out under his supervision. He provided valuable suggestions and helped in reviewing and editing the manuscript.